Journal of The Electrochemical Society, 2021 **168** 060514

Tunable Pseudocapacitive Intercalation of Chloroaluminate Anions into Graphite Electrodes for Rechargeable Aluminum Batteries

Jeffrey H. Xu,[*] Theresa Schoetz, Joseph R. McManus, Vikesh R. Subramanian, Peter W. Fields, and Robert J. Messinger[,z]**

Department of Chemical Engineering, The City College of New York, CUNY, New York, New York 10031, United States of America

---

Rechargeable aluminum-graphite batteries using chloroaluminate-containing electrolytes have been the focus of significant research, particularly due to their high-rate capabilities. Engineered graphite electrodes have been shown to exhibit supercapacitor-like rate performance, despite the fact they store charge via the electrochemical intercalation of polyatomic $AlCl_4^-$ anions. However, the origins of such rate capabilities are not well understood. Here, using electrochemical techniques, we disentangle quantitatively the diffusion-limited Faradaic, pseudocapacitive, and capacitive contributions to charge storage, revealing that $AlCl_4^-$ anions intercalate into graphite with significant pseudocapacitive characteristics due to low ion diffusion limitations. Pristine and mildly exfoliated graphites are compared, where exfoliation resulted in significantly higher pseudocapacitive $AlCl_4^-$ intercalation at the highest potential redox pair as well as higher galvanostatic capacity retention at faster discharge rates. The relationships between graphite structure, ion mass transport, and the overall rate of electrochemical $AlCl_4^-$ intercalation are discussed. Ion diffusion within the electrolyte phase of the porous electrode is shown to play a key role in controlling the rate of intercalation at higher potentials and faster rates, which can be enhanced by reducing electrode tortuosity. The results establish that chloroaluminate anion intercalation into graphite exhibits non-diffusion-limited pseudocapacitive contributions that are tunable by modifying the graphite structure.
[DOI: 10.1149/1945-7111/ac0648]

Manuscript submitted March 3, 2021; revised manuscript received May 16, 2021. Published June 8, 2021. *This was paper 561 presented during PRiME 2020, October 4–9, 2020.*

Supplementary material for this article is available online

Rechargeable aluminum-graphite batteries using chloroaluminate-containing electrolytes are promising candidates for next-generation energy storage: they utilize highly abundant, low cost and inherently safe electrode materials, exhibit an average discharge potential of ca. 2 V vs. Al/Al(III), and are able to to charge and discharge ultrafast.[1–5] The graphite positive electrodes store charge when chloroaluminate $AlCl_4^-$ anions electrochemically intercalate (during charge) and deintercalate (during discharge) via

$$C_n + AlCl_4^- \xrightleftharpoons[\text{discharge}]{\text{charge}} C_n[AlCl_4] + e^- \qquad [1]$$

where $C_n[AlCl_4]$ indicates a graphite-chloroaluminate intercalation compound with a composition that depends on state-of-charge. Researchers have shown that electrochemical properties depend significantly on graphite structure,[6] though the relationship between graphite structure and particular properties of interest, such as rate capability (i.e., capacity retention when cycled at a particular specific current), are still poorly understood. Al-graphite cells using different pristine graphites exhibit varying specific capacities, cycle lifetimes, and rate capabilities, such as pyrolytic graphite foil (66 mAh g^{-1} at 66 mA g^{-1})[1] and natural graphite (120 mAh g^{-1} at 60 mA g^{-1}).[6,7] Most recently, it has been shown that by engineering the graphite structure and/or the composite electrode architecture, the rate capability in particular can be further enhanced, approaching supercapacitor-like performance. For example, Lin et al.[1] developed a vapor-deposited graphitic foam electrode that yielded a capacity of 60 mAh g^{-1} and over 7500 cycles at 4 A g^{-1}, while Chen et al.[5] demonstrated a high-temperature-annealed "graphene film" electrode that yielded a capacity of 111 mAh g^{-1} with 91.7% retention after 250,000 cycles while claiming extremely high specific currents up to 400 A g^{-1}. Later, Shen et al. demonstrated rates as fast as 1,000 A g^{-1} using a graphene cathode that was extensively processed via vapor deposition, acid treatment, and supercritical CO_2 drying, while also modifying the Al anode's grain boundaries with Galinstan "liquid metal."[8] Another economical and scalable method to modify the graphite structure is to exfoliate bulk graphite to decrease the *c*-axis crystallinity.[9,10] For example, Zhang et al. ultrasonicated natural flake-like graphite to exfoliate them into "few-layered graphene," which were used as electrodes that exhibited significantly higher capacity of 75 mAh g^{-1} (compared to 11 mAh g^{-1} for non-exfoliated) at elevated cycling rates of 4800 mA g^{-1}. Graphite exfoliation has also been carried out electrochemically in a sulfate-containing solution, yielding improved rate capabilities with a discharge capacity of 120 mAh g^{-1} at 2 A g^{-1}.[11]

Despite rapid advances in technological performance, researchers have offered different and sometimes conflicting explanations as to how modifying the graphite structure can enhance rate performance. Not surprisingly, the physical origins of such structure-property relationships remain unclear, including a quantitative understanding of which processes are rate-limiting. For example, Ejigu et al. attributed the improved rate capability of electrochemically exfoliated graphite electrodes to "faster ion insertion kinetics," while employing a $CoSO_4$ additive that mitigated surface oxidation.[11] However, unless the chemical compositions of the graphite surfaces are modified significantly, the intrinsic electrochemical kinetics of $AlCl_4^-$ anion intercalation is not expected to change. Another hypothesis that has been offered is that exfoliation increases the intrinsic diffusion of $AlCl_4^-$ anions within the graphite interlayers. Indeed, recent computational studies have suggested that the diffusion coefficient of intercalated $AlCl_4^-$ anions in three-layer graphene (3.4×10^{-7} cm^2 s^{-1}) is ca. 150 times higher than graphite (2.2×10^{-9} cm^2 s^{-1}), which was ascribed to enhanced structural flexibility, though $AlCl_4^-$ interlayer diffusion approaches bulk behavior at approximately 6 layers.[12] To observe this effect in a bulk electrode, the majority of graphite particles would need to be

---

[*] Electrochemical Society Student Member.

[**] Electrochemical Society Member.

[z] E-mail: rmessinger@ccny.cuny.edu

exfoliated to few-layered graphene ($\lesssim$ 6 layers), but this would also result in a significant decrease in capacity attributed to $AlCl_4^-$ intercalation due to fewer available interlayers. In addition, significant capacity would instead arise from $AlCl_4^-$ electrosorption at graphite surfaces (basal planes), which would be expected thermodynamically to occur at potentials different than intercalation. Thus, for many of the Al-graphite systems reported in the literature with modified graphite electrodes, enhanced rate performance is not a consequence of either intrinsically faster electrochemical intercalation kinetics or faster solid-state diffusion of $AlCl_4^-$ anions within the graphite interlayers.

Faster rate performance due to graphite structure modification instead lies in enhanced rates of the overall electrochemical intercalation process, which involves the interplay between ion mass transport and electrochemical kinetics. Physically, the maximum rate is determined by the intrinsic electrochemical kinetics that govern the $AlCl_4^-$ intercalation reaction. Ion mass transport processes can only slow down the overall intercalation process and are often rate-limiting, yielding a slower "apparent" rate. In terms of charge storage mechanisms, the electrochemical intercalation of $AlCl_4^-$ anions into graphite is Faradaic charge storage that results from a redox reaction in which electrons are transferred across an interface. Faradaic charge storage can be further classified into diffusion-limited and non-diffusion-limited charge storage, where the latter is "pseudocapacitive." Pseudocapacitive charge storage thus describes a non-diffusion-limited redox reaction such that the rate of mass transport of the electroactive species to the electrode surface is very fast, compared to the rate of electrochemical intercalation reaction, giving rise to electrochemical responses that have similar characteristics to that of a capacitor. Pseudocapacitive vs diffusion-limited Faradaic contributions thus depend upon the system as well as experimental parameters. True capacitive charge storage, which arises from the physical separation of charges, occurs here within the electrochemical double layer at the electrode-electrolyte interface but is small due to the low surface areas of the graphites.[6] Ion mass transport is negligible for capacitive charge storage.

Technologically, there is great interest to control and enhance pseudocapacitive behavior in batteries to enable energy storage devices with simultaneous high-power and high-energy.[13] Various electrode materials including transition metal oxides,[14] metal organic framework,[15] conductive polymers[16] and carbon-based[17] have demonstrated pseudocapacitive behavior. Indeed, we recently demonstrated that $AlCl_4^-$ anion intercalation into pristine graphite electrodes was not purely diffusion-limited over typical CV scan rates,[6] in contrast with purely diffusion-limited Li^+ cation intercalation into graphite in organic electrolytes.[18] Instead, $AlCl_4^-$ intercalation was either effectively reaction-limited or within a mixed reaction/transport-limited regime, depending on the extent of intercalation (state-of-charge) and graphite type (e.g., natural vs pyrolytic graphite).[6] This result was initially surprising considering the large size of sterically bulky, polyatomic $AlCl_4^-$ ions (5.28 Å diameter)[19] compared to atomic ions such as Li^+ (0.72 Å diameter). But the Al-graphite battery chemistry exhibits many unique features that indicate that electrochemical intercalation of $AlCl_4^-$ is a faster and more facile process than expected. For example, while there have been reports of electrolyte degradation products on the graphite surfaces observed via ex situ characterization methods,[20] there is no evidence to date of a true solid electrolyte interphase (SEI) forming on graphite cathodes in chloroaluminate ionic liquids. Both diffusion limitations and charge-transfer resistance at the electrolyte-electrode interface are expected to be lower in the absence of an SEI. In addition to weak ion desolvation penalties in the electrolyte,[21] we recently revealed via solid-state[22] ^{27}Al NMR spectroscopy that $AlCl_4^-$ anions can intercalate even before the graphite layers expand to form ordered stages by adapting distorted molecular geometries that deviate from tetrahedral configurations, which may play a role in fast rate performance.[23] Meanwhile, computational results predict that solid-state diffusion of $AlCl_4^-$ within the graphite interlayers can occur faster than expected, citing favorably low diffusion barriers,[24,25] the dynamically-changing ion molecular geometries,[23,26] as well as the cooperative movement and change in stacking of the graphene sheets.[27] However, the physical origins of the high-rate capabilities in Al-graphite batteries are still not well understood, including the enhancements obtained by engineering the graphite structure, as there have been no studies to date that have quantitatively disentangled diffusion-limited Faradaic, pseudocapacitive, and capacitive charge storage behavior.

Here, we disentangle the physical charge storage mechanisms and their rate dependencies, revealing that the $AlCl_4^-$ anion intercalation process exhibits significant pseudocapacitive characteristics over common experimental conditions. Using exfoliated graphite as a model material with tunable structure and pristine graphite as a reference, we found that ion mass transport in the porous electrode played a key role in controlling the overall rate of intercalation at higher potentials and faster rates, while pseudocapacitive intercalation can be enhanced by reducing the electrode tortuosity and pore accessibility to the electrolyte. Graphite structures were analyzed with electron microscopy, X-ray diffraction (XRD), X-ray photoelectron spectroscopy (XPS), and nitrogen sorption measurements. Variable-rate galvanostatic cycling and cyclic voltammetry (CV) analyses were conducted to quantify capacity retentions and decouple diffusion-limited Faradaic, pseudocapacitive, and capacitive contributions to the current. Electrochemical impedance spectroscopy (EIS) was used to measure the interfacial charge transfer resistances and apparent ion diffusion coefficients at different states-of-charge, which were rationalized and correlated with the charge storage contributions elucidated by CV analyses. The results yield insights not only into the rate enhancements associated with exfoliated graphite electrodes, but also into the unique electrochemical intercalation process of chloroaluminate anions into graphite electrodes.

Experimental Methods

Graphite exfoliation. Exfoliated synthetic graphite was synthesized via dispersing 100 mg of pristine synthetic graphite powder (TIMCAL, Timrex KS44) in 10 ml of 1-methyl-2-pyrrolidinone (NMP, Fisher Chemical, Lot # 184833) (Fig. S1 (available online at stacks.iop.org/JES/168/060514/mmedia)). Exfoliation was conducted by submerging vials in an ultrasonic bath (Elmasonic P30H) at 80 kHz for 120 min. After exfoliation, the dispersion was centrifuged (Eppendorf 5702) at 3000 RPM (or 1360 × g RCF) for 5 min, yielding smaller particles dispersed in the NMP solvent (light fraction) and larger particles on the bottom and sides of the centrifuge tube (heavy fraction). The light fraction dispersion was removed by pipetting and not used for the electrodes due to low yields. The remaining heavy fraction dispersion was dried at 110 °C under vacuum (4 in Hg) for 12 h to remove the NMP solvent.

Electrode construction and cell assembly. Composite electrodes were constructed using either pristine or exfoliated graphite (heavy fraction only) and polyvinylidene fluoride (PVDF) binder (Sigma-Aldrich, avg. molecular weight 534000 g mol^{-1}) in a mass ratio of 90:10. An electrode slurry was prepared by mixing the graphite and binder with NMP ($\sim$2 ml mg^{-1} of solid material). The electrode slurry was pasted on molybdenum (Mo) foil current collectors (Alfa Aesar, 99.95%, 0.025 mm thick) using a doctor blade set to a thickness of 300 μm. After vacuum drying at 110 °C for 12 h, the dry electrode film thickness was approximately 100 μm. The electrodes used for battery cells were 6-mm diameter disks with an active graphite mass of ca. 1 mg, corresponding to a mass loading of 5 mg cm^{-2}. The porosity of the composite electrodes was estimated to be 50% for both pristine and exfoliated graphites via $1 - \rho_{electrode}/\rho_{materials}$, where $\rho_{electrode}$ is the density of the electrode disk and $\rho_{materials}$ is the tap density of the material components (i.e., 1.9 g cm^{-3} for KS44 graphite and 1.74 g cm^{-3} for PVDF). Cells were assembled in air-tight polytetrafluoroethylene (PTFE) unions (Swagelok, ¼-in (6.35-mm) diameter) under argon atmosphere in a glovebox (<1 ppm O_2 and <1 ppm H_2O) with graphite as the positive electrode, aluminum metal foil (MTI, 99.99%, 0.1 mm thick) as the negative electrode, $AlCl_3$:[EMIm]Cl (Iolitec, 1.5:1 molar ratio) ionic liquid as the electrolyte (30 μl), a fiber glass separator (Whatman GF/D), and molybdenum current collector rods (Torrey Hills Technologies). Open circuit potentials (OCP) were approximately 1.65 V.

Electrochemical cycling. Galvanostatic cycling was performed with an Arbin LBT battery tester with upper and lower potential cut-off limits of 2.45 V and 0.50 V, respectively. Cyclic voltammetry (CV) was performed using a Biologic VSP-300 potentiostat and a two-electrode Swagelok-type cell geometry with aluminum foil as a quasi-reference electrode. Two-electrode cells were used to ensure identical cell geometry between the CV and galvanostatic measurements. Note that two- and three-electrode CV measurement yielded very similar results. Each CV scan began at the OCP followed by increasing potential to the upper limit (2.45 V), down to the lower limit (1.00 V), and then increasing again until the OCP was reached. CV scan rates ranging from 20 $\mu V\ s^{-1}$ to 3 $mV\ s^{-1}$ were used. All electrochemical measurements were performed under ambient temperature. All specific capacities are reported per mass of graphite. Analyses of variable-rate CV peak currents (i_p) were performed by (1) the exponential scaling (*b*-value) method, where i_p was selected as a local maxima that shifts slightly over the range investigated here, and (2) "Dunn's method",[22] which assumes that i_p responses occur at a *fixed* cell potential across different CV scan rates. Thus, small discrepancies may be expected between the exponential *b*-value and the fraction of pseudocapacitive/Faradaic contributions, as a function of cell potential.

Electrochemical impedance spectroscopy. Potentiostatic electrochemical impedance spectroscopy was performed on three-electrode Swagelok-type cells (Fig. S2) using a Biologic VSP-300 potentiostat. Aluminum foils were used as the counter and reference electrodes and graphite was used as the working electrode. An alternating current (AC) amplitude of 10 mV was used and frequencies were varied from 500 kHz to 10 mHz with a sampling of 10 points-per-decade, logarithmically spaced. New cells were first subjected to two CV cycles at a scan rate of 1 mVs^{-1}. Immediately prior to each EIS measurement, linear sweep voltammetry (LSV) at 1 $mV\ s^{-1}$ was used to reach the desired potential (vs. Al/Al(III)) that correspond to CV peaks during charge (1.9 V, 2.0 V, 2.1 V, 2.35 V) and discharge (2.2 V, 1.8 V, 1.7 V). The cell potential was then maintained for 5 min to ensure equilibrium conditions. Total Harmonic Distortion (THD) and the Non-Stationary Distortion (NSD) analyses were conducted to test the causality/linearity and stability of the EIS measurements, respectively, which varied by less than 5% across the entire frequency range (Fig. S3).[28]

Galvanostatic intermittent titration technique. Cells were first subjected to three galvanostatic discharge/charge cycles at 60 $mA\ g^{-1}$ prior to any GITT measurements. Galvanostatic pulses at 60 $mA\ g^{-1}$ were applied for 300 s using potential cutoffs of 2.45 V and 0.5 V during charging and discharging, respectively. The rest duration between pulses for both charging and discharging was 3 h. The internal resistance (IR) of the cell was measured at the beginning of each current pulse using the Arbin IR-control algorithm, which generates 10 current pulses of 20 ms with amplitudes of ±60 $mA\ g^{-1}$.

Electron microscopy. A FEI Titan Themis 200 kV transmission electron microscope (TEM) was used to probe the nanoscale structures of pristine and exfoliated graphites. Graphite samples were dispersed in ethanol, transferred to a TedPella lacey carbon 400 mesh grid, and then vacuum dried at 60 °C for 2 h.

X-ray diffraction. An X'Pert powder X-ray diffractometer equipped with a Cu K-α radiation source (λ = 0.154 nm) was used to measure long-range periodic ordering of the graphites. A scan rate of 0.5° (2θ) min^{-1} was used to scan a 2θ range of 20°–60°.

X-ray photoelectron spectroscopy. A PHI Versaprobe II X-ray photoelectron spectrometer with Al Kα X-rays ($h\nu$ = 1,486.6 eV, spot size = 200 μm, 45° measuring angle) was used to analyze surface compositions of the graphite particles. Pristine graphite was soaked in NMP for 2 h (without ultrasonication) and then dried at 110 °C under vacuum (4 in Hg) for 12 h so that the results can be directly compared to those of exfoliated graphite. The source potential and emission current were 15 kV and 4 mA, respectively. Adventitious carbon was removed from the samples via Ar^+ irradiation for 10 min at 1 keV. Deconvolution of the C1s spectrum was performed with the PHI MultiPak software using a Shirley background subtraction.

Nitrogen sorption. A Micromeritics ASAP 2020 adsorption analyzer was used to conduct N_2 sorption measurements to measure the specific surface area and pore volumes of pristine and exfoliated graphite powders. The pristine graphite was dispersed in NMP and soaked for 2 h, then dried at 110 °C under vacuum (4 in Hg) to subject it to the same treatment as the exfoliated graphite so that it can be directly compared to exfoliated graphite. The samples were degassed at 150 °C for 12 h prior to isotherm determination in the relative pressure range of $0.1 < P/P_0 < 1.0$. The BET specific surface area was determined using the isotherm range of $0.1 < P/P_0 < 0.3$, while the pore volume was determined at $P/P_0 = 0.990$ using Gurvich's rule,[29] which assumes that the adsorbed N_2 condenses inside the pores at $P/P_0 \approx 1.0$.

Results and Discussion

Structures & surface compositions of graphites.—The effects of mild liquid-phase ultrasonic exfoliation on graphite structure and surface composition were revealed by transmission electron microscopy (TEM), X-ray diffraction (XRD), X-ray photoelectron spectroscopy (XPS) and BET N_2 sorption analyses (Fig. 1). TEM revealed that pristine synthetic graphite exhibits a highly crystalline, layered structure of stacked graphene layers along the *c*-axis (Fig. 1a), as expected. After exfoliation and centrifugation of pristine graphite, two types of exfoliated graphite (light and heavy fractions) were generated. Heavy fraction particles exhibited thinner crystallite heights and some folding at flake edges (Fig. 1b). The light fraction, which consisted of thinner and/or laterally smaller flakes that were cleaved off of bulk particles (Fig. S4), was separated via centrifugation and not used in the electrode due to low yields. For both graphite types, Moiré fringes were observed due to interference of overlap crystallites with different rotational orientations (Figs. 1a, 1b). XRD yielded a characteristic diffraction pattern of graphitic carbon for both the pristine and exfoliated samples (Fig. 1c), as indicated by the negligible change in the position of the (002) reflection at ca. $2\theta = 26°$ upon exfoliation. XRD thus establishes that mild ultrasonic exfoliation preserves sufficient long-range molecular-scale ordering of the graphite structure, as few-layered or monolayer graphene would result in the absence of the interlayer (002) reflection. No graphene oxide was observed, as evidenced from the lack of a characteristic graphene oxide peak at $2\theta = 11°$.[30]

XPS was used to quantify the relative sp^2 and sp^3 carbon bonding environments, as well as characterize the oxygen defects, on the graphite surfaces (Figs. 1c, 1d). Deconvolution of the C1s photoelectron spectrum revealed three components: (i) an asymmetric peak (80% Gaussian) centered at ∼284 eV attributed to sp^2 carbons that are characteristic of ordered graphite, (ii) a symmetric peak (95% Gaussian) centered at ∼285 eV attributed to sp^3 carbons that are associated with dangling, terminal C–C bonds at edge sites[31] and (iii) a symmetric peak (100% Gaussian) centered at ∼289 eV that is likely associated with C=O and/or O–C=O states[32] at edge sites, indicating the presence of oxygen defects as well as residual NMP solvent. Within experimental and fitting error, the relative concentrations for each component are the same for pristine and exfoliated graphite, establishing that the mild exfoliation treatment does not modify the surface chemistry of the graphite particles.

Nitrogen sorption measurements (Fig. S5a) were used to analyze the surface area and pore volumes of the raw graphite materials. The similar Type II isotherms of pristine and exfoliated graphite indicated that the two materials possess similar nonporous structures

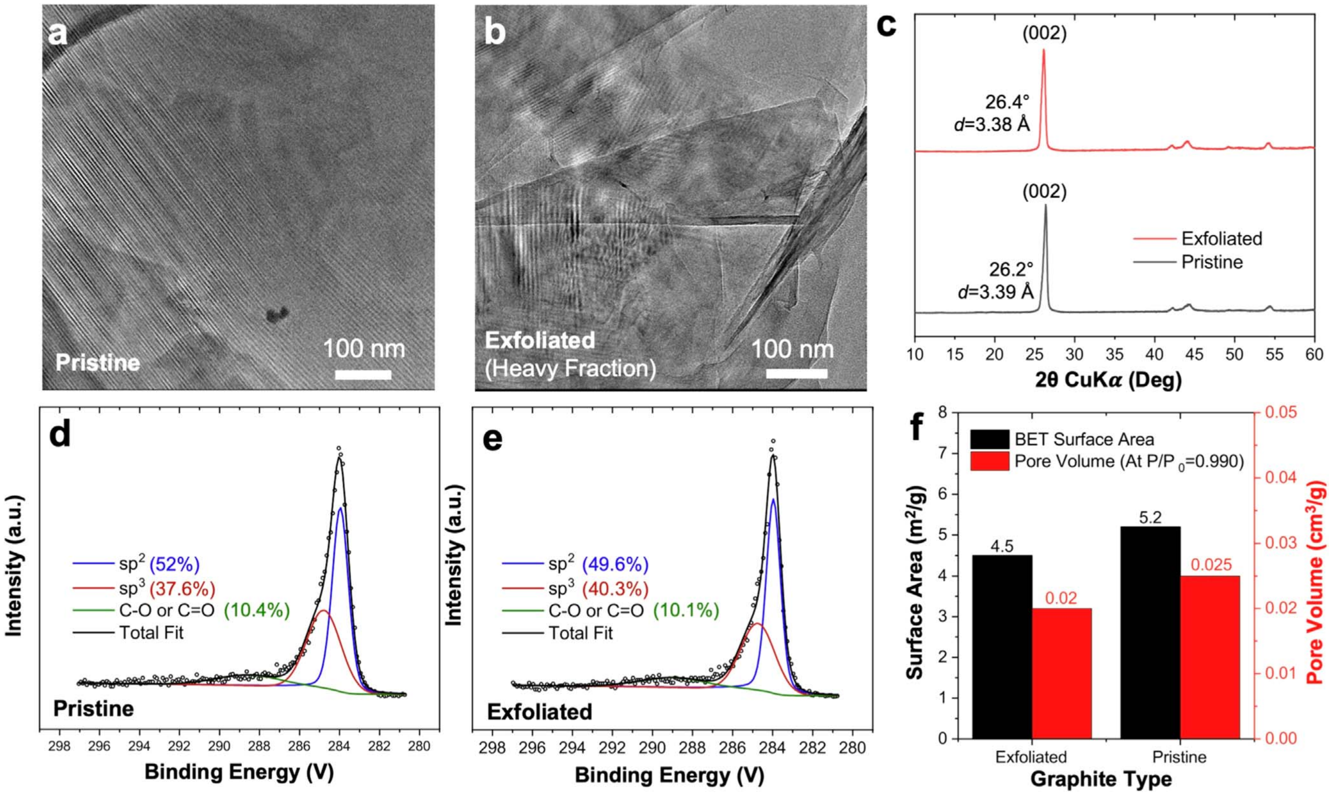

Figure 1. Comparison of the structures and surface compositions of pristine and exfoliated graphites. TEM images of (a) pristine and (b) exfoliated graphite. (c) XRD patterns. XPS binding energies (carbon region) of (d) pristine and (e) exfoliated graphite. (f) Specific surface areas and pore volumes obtained by N_2 sorption isotherms.

and gas adsorption properties.[29] Brunauer–Emmett–Teller (BET) analysis of the isotherm (Fig. 1f) yielded similar specific surface areas for pristine graphite (5.2 m^2 g^{-1}) compared to exfoliated graphite (4.5 m^2 g^{-1}). Likewise, the pore volume was estimated to be similar for pristine graphite (0.025 cm^3 g^{-1}) than for exfoliated graphite (0.020 cm^3 g^{-1}). Thus, while mild exfoliation process alters the *c*-axis thickness, it does not significantly alter the specific surface area or total pore volume associated with interparticle void spaces. Additionally, BJH pore size distributions of pristine and exfoliated graphites show similar distributions for both graphite types (Fig. S5b). However, these pore size distributions should be used solely for comparing the graphite types, as opposed to detailed quantitative interpretations, since BJH pore size analyses are of limited accuracy for non-microporous materials such as the pristine and exfoliated graphite investigated here.

Electrochemical cycling of Al-graphite cells.—Electrochemical cycling of pristine and exfoliated graphite cathodes revealed similar electrochemical behavior and cell-level performance at lower rates, but significant differences at faster rates. At a relatively slow galvanostatic cycling rate (60 mA g^{-1}), both pristine and exfoliated graphite yielded identical specific discharge capacities (78 mAh g^{-1}), indicating a similar number of accessible intercalation sites. A discharge capacity of 78 mAh g^{-1} corresponds to an estimated average composition of $C_{28}[AlCl_4]$,[6] neglecting ion trapping that occurs during the first cycle.[23] Furthermore, both graphite types exhibited graphite staging transitions at nearly identical cell potentials,[1,2,6,33] as shown by their similar differential capacity curves (Fig. 2b) and cyclic voltammograms (Fig. 2c). The results establish that after exfoliation, the structure remains sufficiently crystalline to support intercalation reactions with periodic graphite staging. To test the hypothesis that exfoliation

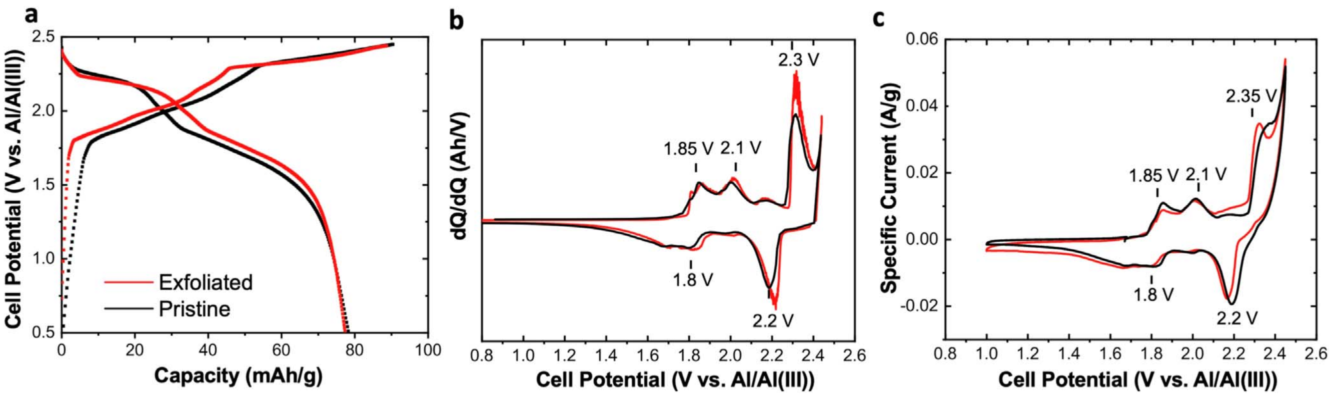

Figure 2. Electrochemical characterization of Al-graphite cells containing pristine or exfoliated graphite cathodes via (a) galvanostatic cycling at 60 mA g^{-1} (5th cycle), (b) the corresponding differential capacity analysis, and (c) CV at 20 μV s^{-1} (3rd scan).

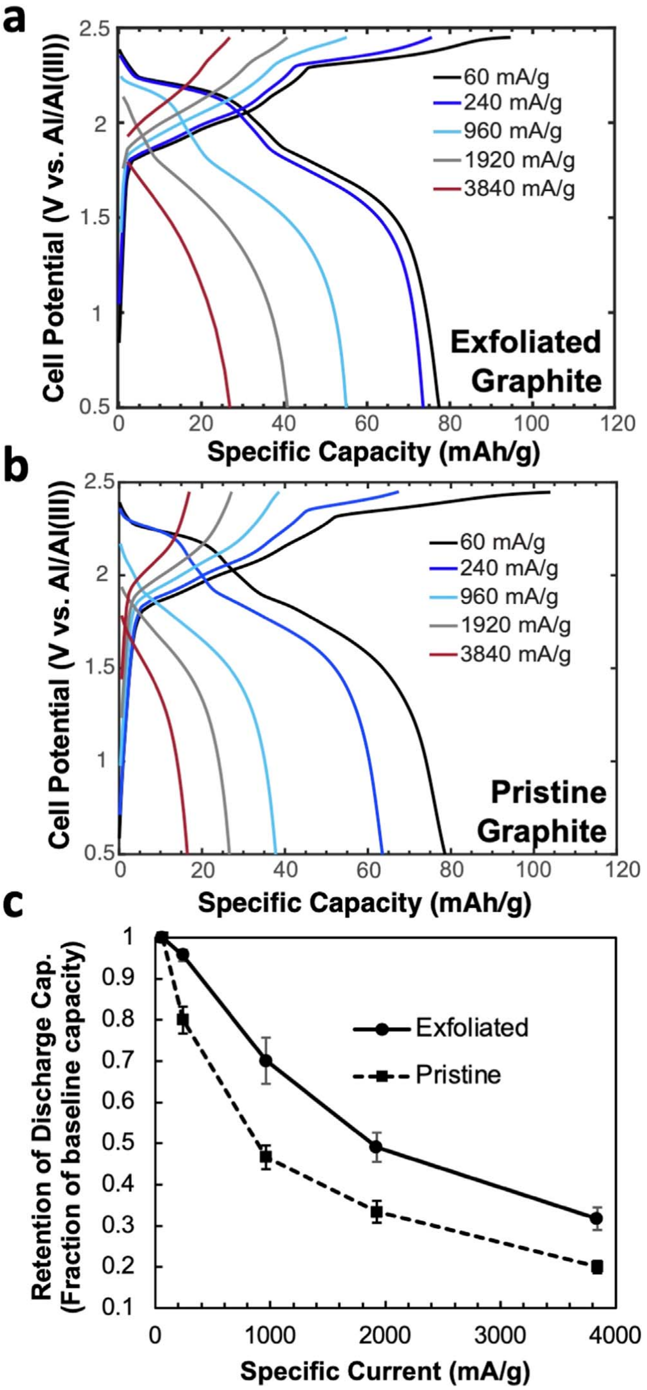

Figure 3. Galvanostatic cycling as a function of increasing specific current for Al-graphite cells containing (a) exfoliated and (b) pristine graphite. For each rate, the 10th cycle is shown. (c) Fraction of retained discharge capacity with increasing specific current. Uncertainty bars represent the standard deviation about the mean value of 3 cells.

enhances rate capability, variable-rate galvanostatic cycling was conducted at rates ranging from 60 to 3800 mA g^{-1} (Figs. 3a, 3b). Above 60 mAh g^{-1}, exfoliated graphite showed a higher retention of specific discharge capacity. For example, at 960 mA g^{-1}, exfoliated graphite yielded an average 70% capacity retention, higher than the 47% capacity retention for pristine graphite at the same rate (Fig. 3c). Insights into the higher-rate performance behavior of exfoliated graphites were elucidated using variable-rate cyclic voltammetry (Figs. 4a, 4b). At slow rates (e.g., 20 μV s^{-1}), the CVs of exfoliated and pristine graphite were very similar (Fig. 2b). However, CVs obtained at faster scan rates of 3 mV s^{-1} (Figs. 4c, 4d, black line) showed that exfoliated graphite exhibits significantly higher specific current at the 2.3 V/2.2 V charge/discharge couple compared to pristine graphite, consistent with the higher degree of pseudocapacitive behavior in the exfoliated materials at these potentials, as shown below.

Electrochemical analyses of charge storage mechanisms & effects of ion mass transfer.—Faradaic and (pseudo)capacitive charge storage processes were disentangled by analyzing how the CV peak current (i_p) scales with the CV sweep rate (v) according to[22,34]

$$i_p = av^b \qquad [2]$$

where b is an exponential scaling term between 0.5 and 1. Electrochemical processes that exhibit the square-root scaling $i_p \sim v^{0.5}$ ($b = 0.5$) are Faradaic reactions that are completely diffusion-limited, whereas the linear scaling $i_p \sim v$ ($b = 1$) indicates either capacitive and/or pseudocapacitive behavior, where the latter are simply Faradaic reactions that are non-diffusion-limited (i.e., reaction-limited). Note that this scaling analysis cannot distinguish the similar electrochemical responses of pseudocapacitive and capacitive behavior, so we denote the combination of the two as "(pseudo)capacitive." However, the true capacitive contribution arising from electric double layer (EDL) charging can be quantified via first integrating the CV curve with respect to time across a region ΔE where the current is constant (flat region) and scales like $i_p \sim v$(here, ΔE from 1.0–1.5 V, cathodic scan), yielding the charge Q arising from the EDL within this region. The specific capacitance C, which is a constant, can then be calculated according to $C = Q/\Delta E$. Both pristine and exfoliated graphites had a specific capacitance C of 2 mF m^{-2}. This specific capacitance is independent of potential and can therefore be applied to the entire potential window of the CV (1.0–2.45 V).

As shown below, pseudocapacitive contributions to the current are dominant over EDL capacitive contributions, establishing that any non-diffusion-limited behavior is indeed a result of the Faradaic electrochemical intercalation of $AlCl_4^-$ anions into graphite.

Overall, applying this scaling analysis to key CV peaks reveals a striking difference between the two graphite types (Figs. 4a, 4b). In particular, pristine graphite exhibited only diffusion-limited Faradaic charge storage ($b = 0.5$) at the high-potential charge/discharge couple (2.35 V/2.2 V) (Fig. 4b), while charge storage in the exfoliated graphite was almost reaction-limited and thus pseudocapactive ($b = 0.9$, Fig. 4a). This result is technologically interesting as capacity retention is most important at higher potentials. At all other states-of-charge, both graphite types exhibited a mix of (pseudo)capacitive and diffusion-limited Faradaic and behavior ($0.8 < b < 0.9$).

The different charge storage mechanisms can be further quantitatively decoupled as a function of potential by expanding on the current scaling relationships noted above. Mathematically, the total current can be expressed as a linear combination of (pseudo) capacitive and diffusion-limited Faradaic contributions via[22]

$$\frac{i_{tot}}{v^{0.5}} = k_1 v^{0.5} + k_2 \qquad [3]$$

where k_1 and k_2 represent the fraction of current that exhibits a (pseudo)capacitive and diffusion-limited Faradaic electrochemical response, respectively. These contributions k_1 and k_2 can be calculated from the slope and y-intercept, respectively, of the linear regression of the total current $i_{tot}/v^{0.5}$ vs the square-root of the CV sweep rate $v^{0.5}$. Consequently, this analysis enables quantitative deconvolutions of the CVs into (pseudo)capacitive and diffusion-limited Faradaic current contributions (Figs. 4c, 4d). At a faster CV scan rate of 3 mV s^{-1}, for example, the integrated charge contributions for exfoliated graphite was 76% pseudocapacitive ($Q_{pseudo} =$ 318 mAs), 17% diffusion-limited Faradaic ($Q_{Faradaic} = 71$ mAs) and

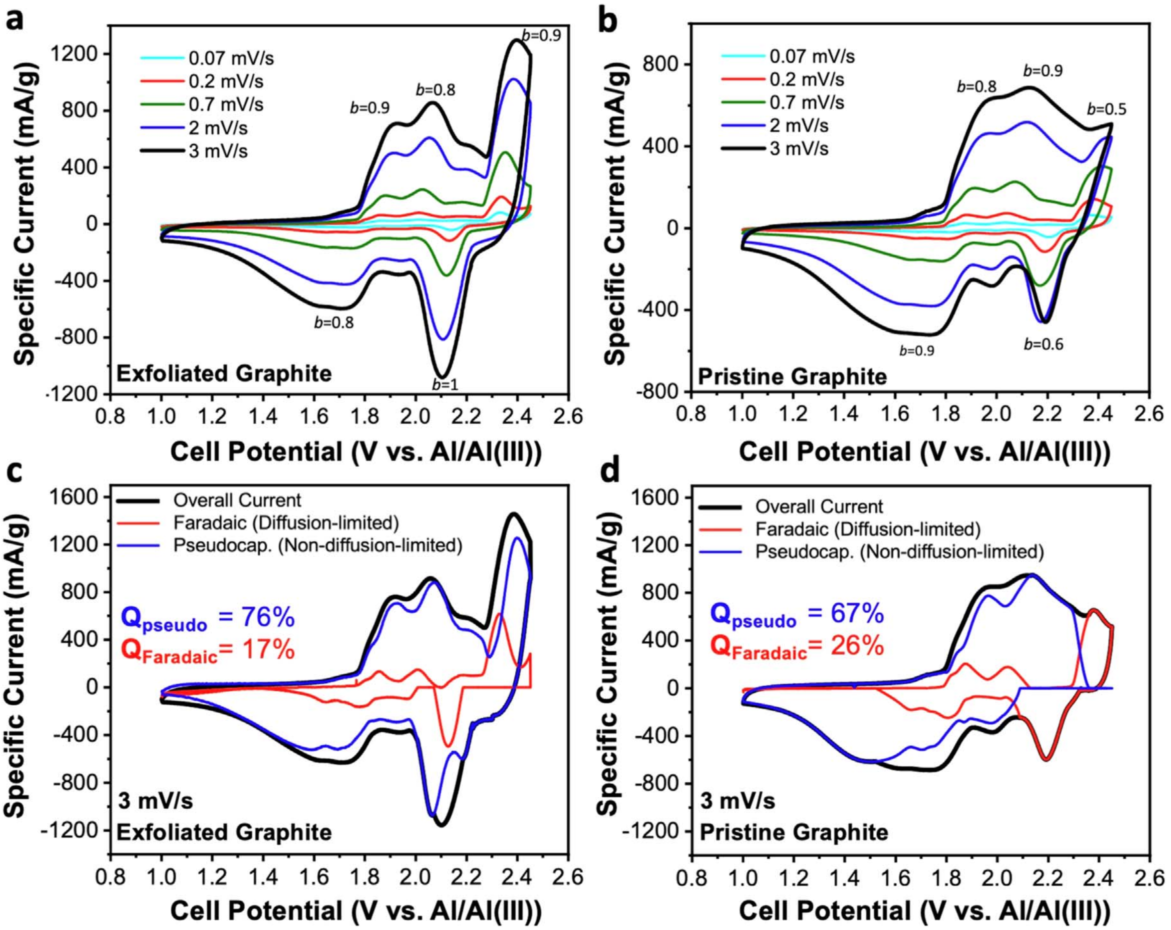

Figure 4. CVs conducted at increasing scan rates (0.07–3 mV s^{-1}) on Al-graphite cells containing (a) exfoliated and (b) pristine graphite cathodes. (a)–(b) The "*b*-values" were calculated by tracking the relative maxima of current peaks at select cell potentials. The fast CV scan (3 mV s^{-1}) was analyzed to decouple non-diffusion-limited pseudocapacitive and diffusion-limited Faradaic contributions to the overall current for (c) exfoliated graphite and (d) pristine graphite.

7% capacitive (Q_{EDL} = 28 mAs). Exfoliated graphite exhibited a larger total pseudocapacitive contribution than pristine graphite (76% vs 67%) and consequently less diffusion-limited Faradaic contributions (17% vs 26%), where the main differences occur at higher potentials. Indeed, exfoliated graphite exhibited significantly greater pseudocapacitance at the high-potential coupled peaks (2.2/2.3 V) that account for approximately 30% of the total capacity (at 3 mV s^{-1}), consistent with the scaling analysis above. Note that the true capacitive contributions are small (7%), an expected result due to the low specific surface areas (ca. 5 m^2 g^{-1}, Fig. 1f) of the graphites compared to their total theoretical interlayer surface area.[6] Overall, these results are consistent with mild exfoliation: anions can more easily diffuse to and access the intercalation sites at the graphite particle edges, including at high rates.

EIS measurements were performed at key states-of-charge corresponding to CV peak maxima to further characterize the interplay of pseudocapacitive and diffusion-limited Faradaic processes that occurs during the electrochemical intercalation of $AlCl_4^-$ anions into graphite. The impedance data are represented in complex plane (Nyquist) plots (Figs. 5a–5d), where $Z'(\Omega)$ and $Z''(\Omega)$ are the real and imaginary components of the complex impedance, respectively. Equivalent circuit analysis was performed with a simple circuit model (Fig. 5e) which comprises a (i) resistor (R_1) to model inner cell resistances (e.g., due to electrolyte and separator), (ii) a constant phase element[35] (Q) along with a resistor (R_2) in parallel to model the charge transfer resistance of the electrode-electrolyte interface[35] and (iii) a modified Warburg element[36] (M_α) to model the finite-length ionic diffusion occurring between the surface edge planes and bulk interlayers. The inner resistances (R_1) were determined to be ∼15 Ω for both graphite types. Note that a constant phase element, instead of an ideal capacitor, was used to account for heterogeneities arising from pore and particle size distributions[37] as well as surface energy distributions due to disorder at edge sites.[38] The modified (finite-diffusion) Warburg element was used to model the low-frequency EIS data instead of the semi-infinite Warburg element, as the low-frequency tail deviated significantly from the 45° slope that indicates semi-infinite diffusion. Note that the modified Warburg element has been used to model finite-length diffusion in other ion insertion electrodes.[36,39]

The EIS data reveal significant differences between graphite type and state-of-charge in the (i) diameter of the semi-circle, linked to interfacial charge transfer resistance, and (ii) slope of the low-frequency "tail" due to varying ion mass transport limitations. During charging, when $AlCl_4^-$ anions electrochemically intercalate into the graphite, the increasing ionic concentration gradient in the bulk porous electrode yields a higher charge transfer resistance at the electrode/electrolyte interface, as shown by the increasing semi-circle diameters (R_2, Table SI). Between graphite types, the interfacial charge transfer resistance was smaller for exfoliated graphite than for pristine graphite. For example, at 2.35 V, exfoliated graphite yielded a lower resistance (R_2 = 29 Ω) than pristine graphite (R_2 = 39 Ω). This lower resistance is directly linked to the increased pseudocapacitive behavior (Faradaic non-diffusion-limited intercalation) revealed above in the exfoliated graphite. It is thus apparent that the exfoliation process alters the graphite structure in a way that minimizes ion concentration gradients and hence enhances diffusive flux. Due to greater pseudocapacitive contributions, the corresponding magnitude of the constant phase element parameter Q

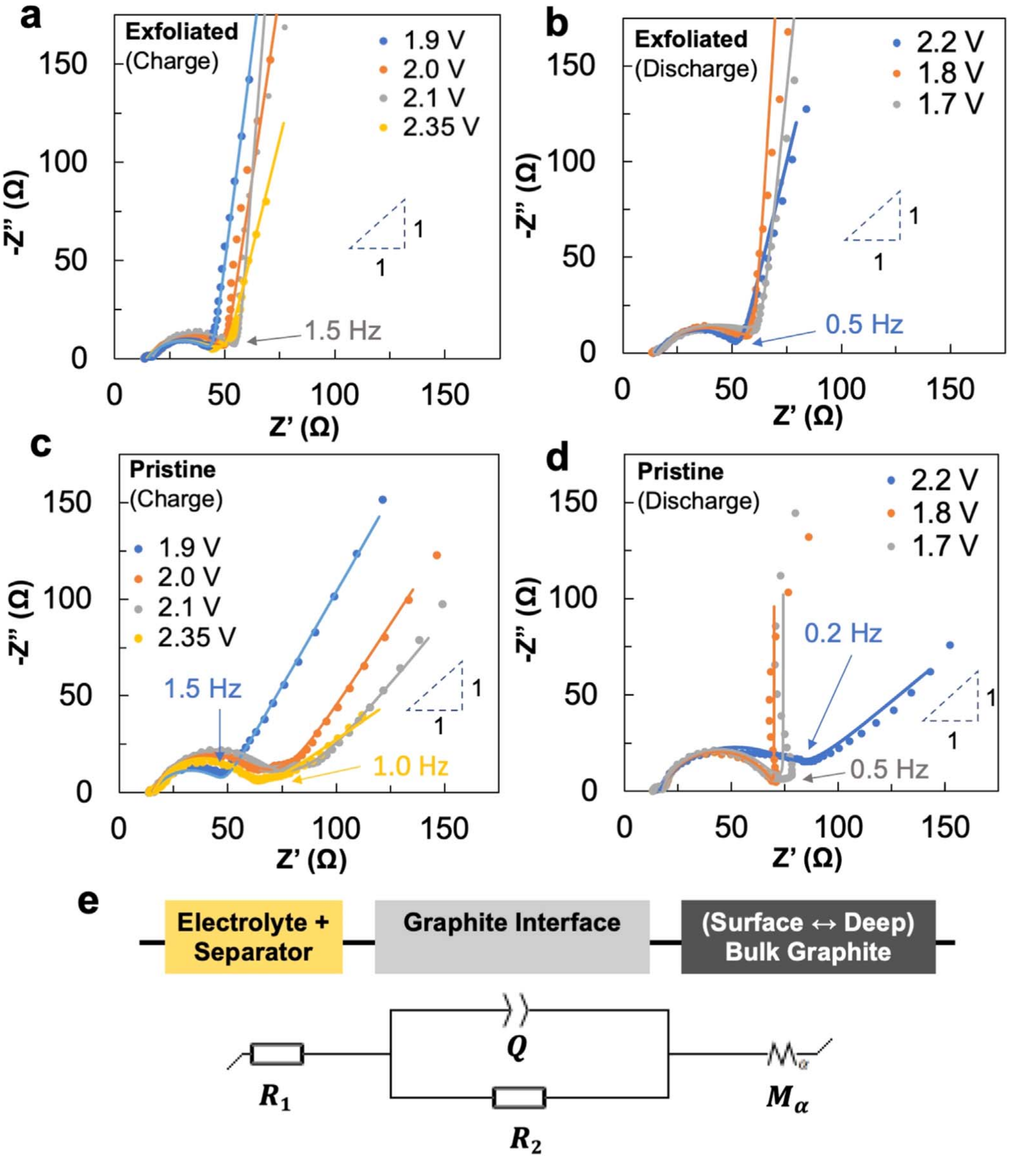

Figure 5. Nyquist plots of EIS experiments conducted at various states-of-charge for Al-graphite cells containing (a)–(b) exfoliated and (c)–(d) pristine graphite cathodes. Annotated frequency values refer to the point at the "elbow" formed by the semi-circle and the linear tail. Solid lines are fits from the equivalent circuit model (e).

was orders-of-magnitude higher for exfoliated graphite ($Q = 1.19 \times 10^{-3}\ \mathrm{F\,s^{-1}}$) compared to that of pristine graphite ($Q = 6.21 \times 10^{-6}\ \mathrm{Fs^{-1}}$). Additionally, the deviation from a perfect semi-circle shape is described by the depression factor α ($-1 < \alpha < 1$; derived from the CPE element). Overall, at all cell potentials, exfoliated graphite exhibited modestly higher depressions of the semi-circle ($0.61 < \alpha < 0.71$, Table SI) than pristine graphite ($0.75 < \alpha < 0.88$). The depression of the semi-circle (i.e., a lower α value) is typically attributed to pseudocapacitive contributions.[37] Next, analyzing the low-frequency tail of the Nyquist curves that corresponds to the timescale at which ion diffusion occurs, exfoliated graphites exhibit slopes of ~82° during charging at 1.9, 2.0, and 2.1 V, and ~75° at 2.35 V (Fig. 5a), consistent with the pseudocapacitive contributions shown by variable-rate CV analysis (*b*-values of 0.8 to 0.9, Fig. 4c). On the other hand, pristine graphite exhibits a lower-sloped tails of ~50°–60° during charging at 1.9, 2.0, and 2.1 V, and ~40° at 2.35 V (Fig. 5c), indicating higher diffusion-limitations. This result suggests that $\mathrm{AlCl_4}^-$ intercalation in the region defined by the edge plane to the deep interlayers of the graphite particle is more facile for exfoliated graphite (Fig. 5b), which is quantitatively interpreted below via the apparent diffusion coefficient D_{EIS}.

EIS also revealed the interfacial and transport behavior during the discharge process, where ions are either (i) deintercalating from the edges into the bulk electrolyte or (ii) diffusing through the bulk interlayers towards the edge sites. At a cell potential of 2.2 V, pristine graphite exhibits a nearly 45°-sloped (Fig. 5d) low-frequency tail and a significantly higher charge transfer resistance ($R_1 = 60\ \Omega$) than that of exfoliated graphite (~75° slope, $R_1 = 38\ \Omega$). This result establishes that diffusion-limited mass transport is more prevalent than pseudocapacitive deintercalation at the edges of pristine graphite, consistent with the diffusion-limited square-root scaling $b = 0.5$ observed in the CVs above (Fig. 4d). Interestingly, after further discharge to 1.8 V and 1.7 V, pristine graphite exhibits a nearly vertical low-frequency tail that resembles an ideal capacitor. The ions that have diffused out of the interlayers accumulate at the electrode surface due to high diffusion limitations in the pores. This effectively traps the ions remaining in the graphite over this time scale, while any additional ion transport resembles capacitive double-layer discharging (also shown by Bode plot, Fig. S6, discussed below). Exfoliated graphite, on the other hand, maintains lower charge transfer resistances as shown by smaller semi-circle diameters. Also, overall lower diffusion limitations are observed as shown by higher slopes in the low-frequency region during discharge at all cell potentials tested (Fig. 5b), except at 1.8 V and 1.7 V where pristine graphite exhibits capacitive double-layer discharging as evidenced by the nearly-vertical slopes at 1.8 V and 1.7 V (Fig. 5d).

The phase angle (ϕ), represented by Bode plots as a function of frequency (Fig. S6), is another parameter that reveals the different charge storage contributions. The phase angle ϕ is defined as

$$\phi = \tan^{-1}\left(\frac{Z'(\omega)}{Z''(\omega)}\right) \qquad [6]$$

Certain values of ϕ indicate Faradaic (diffusion-limited or pseudocapacitive) or capacitive charge storage. A phase angle of $\phi = -90°$ represents (pseudo)capacitive intercalation, while an angle of $\phi = -45°$ (consistent with the Warburg element) represents diffusion-limited Faradaic intercalation.[40] For example, at low-frequencies where mass transport processes are dominant (e.g., 0.01 Hz), exfoliated graphite exhibits a greater (pseudo)capacitive response ($|\phi|>45°$) than pristine graphite at all measured cell potentials (Fig S6a,b). At 0.01 Hz, pristine graphite exhibited phase angles nearer to $\phi = -45°$ (Fig S6c,d), indicating diffusion-limited Faradaic behavior. Additionally, a phase angle of $\phi = 0°$ represents pure resistive behavior in which there is little or no ionic movement.[40] Analyzing the higher-frequency segments of the Bode curves during charging, the phase angle of pristine graphite reaches an asymptotically low value ($|\phi|<10°$) at a lower frequency (e.g., 0.05 Hz at 2.35 V, Fig. S6g) compared to exfoliated graphite (e.g., 0.26 Hz at 2.35 V, Fig. S6c), which is consistent with the fact that greater charge transfer resistances are observed over a wider range of timescales for pristine graphite (also represented by the larger semicircles in Figs. 5c, 5d). Note that the anomalous capacitive behavior observed for pristine graphite during discharge at 1.8 V and 1.7 V is consistent with the rapid decrease to $\phi = -5°$ with increasing frequency, suggesting virtually no ion movement after the initial capacitive discharging (Fig. S6h).

The apparent diffusion coefficient of $AlCl_4^-$ anions within the composite graphite electrodes was estimated using EIS. Note that GITT measurements are another common method to estimate ion diffusion coefficients in battery electrodes. However, since GITT models assume pure diffusion limitations, GITT analyses will *not* accurately quantify ionic diffusion associated with $AlCl_4^-$ intercalation into graphite due to the significant non-diffusion-limited pseudocapacitive processes elucidated above. Nevertheless, as an exercise for comparison, GITT measurements were performed for both graphite types (Fig. S7) and the apparent diffusion coefficients D_{GITT} (Fig. S8) are discussed in the Supporting Information (Text S1, Table SII). EIS, however, can in principle take into account both pseudocapacitive and diffusion-limited Faradaic contributions by modeling the mid-frequency semi-circle and low-frequency "tail."[36] To account for the significant deviation of the low-frequency tail from a 45° slope indicative of semi-infinite diffusion, the finite-length modified Warburg circuit element was used to estimate the characteristic diffusion time τ_d corresponding to the EIS frequency range of $f < 1.5$ Hz (Fig. 5). If the characteristic diffusion length L is known, the order-of-magnitude of the apparent ion diffusion constant D_{EIS} can be estimated via the scaling relationship $D_{EIS} \sim L^2/\tau_d$. More specifically, L is the length scale over which ion concentration gradients occur. As discussed below, ion transport in the electrolyte phase within the porous electrode must play a critical role in controlling the diffusion limitations, particularly at higher potentials and cycling rates; solid-state ion diffusion within the graphite interlayers may indeed still play a role in the overall rate of $AlCl_4^-$ intercalation, but it alone cannot account for the faster rate performance and greater apparent diffusion coefficients of exfoliated graphite, compared to pristine graphite. Determination of the correct length scale L is not clear as concentration gradients may exist in both the liquid electrolyte and solid graphite phases, but assuming an average characteristic diffusion length scale of 10^{-5} cm, for example, the calculated D_{EIS} values range from 10^{-12} to 10^{-10} cm^2 s^{-1}, depending on state-of-charge and graphite type (Table SIII). Due to the uncertainty in L, only the trends in D_{EIS} are analyzed here. Between graphite types, exfoliated graphite exhibits higher apparent ion diffusion coefficients, confirming that exfoliated graphite facilitates faster overall ion mass transport than pristine graphite. During charge (intercalation), apparent diffusion coefficients for exfoliated graphite are constant at potentials of 2.1 V and below, decreasing an order-of-magnitude at the higher potential of 2.3 V. During discharge (deintercalation), apparent diffusion coefficients decrease modestly, less than one order-of-magnitude, as the potential decreases. Apparent ion diffusion coefficients are calculated for different values of the characteristic diffusion length (e.g., $10^{-6} < L < 10^{-3}$ cm), which yield identical trends but vary only in magnitude according to the scaling $D_{EIS} \sim L^2$ (Fig. S9).

Relationship between graphite structure, ion mass transport, and rate of $AlCl_4^-$ electrochemical intercalation.—In aggregate, the electrochemical methods above establish that the electrochemical intercalation of $AlCl_4^-$ anions into graphite exhibits significant pseudocapacitive contributions over common experimental conditions as a result of non-diffusion-limited ion intercalation processes. Furthermore, ion diffusion limitations that do exist can be reduced, and consequently rate performance enhanced, by modifying the graphite structure. The electrochemical differences observed between pristine and exfoliated graphites cannot be explained by differences in solid-state ion diffusion within the graphite interlayers, as argued above, as this would require few-layered graphene (less than approximately 5 or 6 layers) instead of bulk graphene. Between the pristine and exfoliate graphites studied here, the specific surface areas, electrode porosities, and surface chemistry are similar. True EDL capacitive contributions are small, consistent with the low specific surface areas of the graphites. The significant differences in rate performance, then, must be due to ion mass transport in the electrolyte phase within the porous electrode structure. This result reveals one key difference between Al-graphite batteries and other common battery intercalation electrodes and chemistries (e.g., Li^+ intercalation into graphite), which are typically rate limited by solid-state ion diffusion and not ion transport in the electrolyte. Diffusion in porous media follows the well-established relationship[41]

$$D_{eff} = D_{bulk} * \frac{\phi}{\tau} \qquad [7]$$

where D_{eff} is the effective ion diffusion coefficient within the porous structure, D_{bulk} is the ion diffusion coefficient in the bulk electrolyte, ϕ is the electrode porosity, and τ is tortuosity. D_{bulk} is 4.45 * 10^{-6} cm^2 s^{-1} for $AlCl_4^-$ anions in the neat electrolyte[42] while ϕ is ca. 0.50 (calculated above). The porous electrode structure is also described by its tortuosity (τ), a parameter that reflects the curvature and efficiency of percolating pathways within the material. Since D_{bulk} and ϕ are unchanged upon exfoliation, we conclude that the tortuosity τ must decrease, thereby increasing the efficiency of ion transport pathways and enhancing the diffusive flux of ions to the graphite surfaces.

The exfoliated and pristine graphites thus exhibit key differences in their structures that influence how ion mass transport affects the overall rate of electrochemical $AlCl_4^-$ intercalation, which are summarized in Fig. 6. Mild exfoliation reduces the *c*-axis thickness of graphite particles and facilitates a graphite particle arrangement whose porous structure reduces ion mass transport limitations. In addition to (i) reduced tortuosity, which increases the effective diffusion coefficient of $AlCl_4^-$ anions within the porous electrodes, we hypothesize that there is also (ii) increased accessibility of interstitial pores to $AlCl_4^-$ anions and a concomitant reduction of small nanopores, which otherwise could become locally depleted,

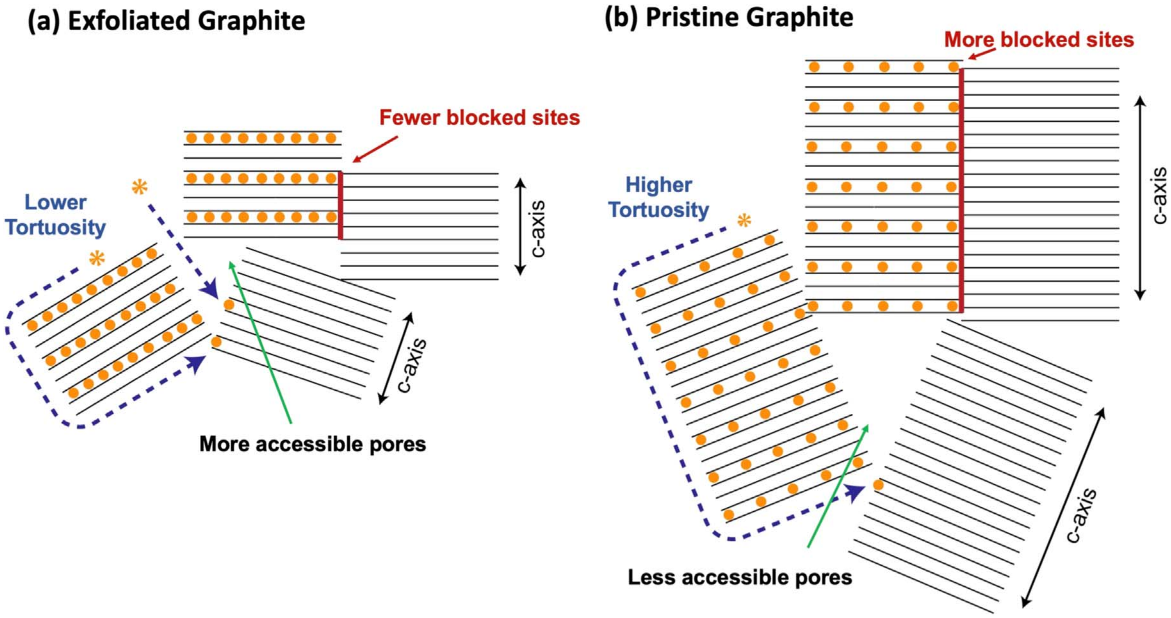

Figure 6. Schematic depicting key features of graphite structure that affect ion mass transport and hence the apparent rate of $AlCl_4^-$ anion intercalation in (a) exfoliated and (b) pristine graphite.

generating ion concentration gradients and hence diffusion limitations, as well as (iii) fewer blocked edge sites due to graphite particles in close proximity. Pertaining to the Al-graphite battery chemistry itself, the solid-state diffusion of $AlCl_4^-$ anions into graphite appears to be anomalously fast; if it were slow compared to the rates of ion diffusion within the porous electrode and electrochemical insertion kinetics, then it would be rate-limiting. Regarding ion insertion, the lack of a reported SEI on the graphite cathode combined with the weak desolvation penalties of $AlCl_4^-$ anions in the ionic liquid electrolyte facilitate fast $AlCl_4^-$ insertion at the electrolyte-electrode interface. Here, mild exfoliation was performed to study the $AlCl_4^-$ intercalation process into a model graphite material, while pristine graphite served as a reference. One technological advantage of ultrasonic exfoliation is that it is scalable and permits the manufacture of electrodes with high mass loadings. Graphite electrodes can be further engineered to reduce diffusion limitations and enable ultra-fast rate performance, which has been demonstrated in highly oriented and porous graphene-type structures using high-temperature, high-pressure and acid dissolution treatments.[5,8] An interesting direction of future research would be to engineer the graphite structure to further reduce ion diffusion limitations while enabling electrodes with high mass loadings and electrode densities.

Conclusions

Charge storage mechanisms in graphite electrodes for rechargeable aluminum-graphite batteries were quantitatively decoupled into diffusion-limited Faradaic, pseudocapacitive, and capacitive contributions. Two graphite types were studied: pristine graphite and exfoliated graphite prepared by mild ultrasonication. Galvanostatic cycling and CVs established effectively identical capacities and CV redox peaks between the two graphite types at slower rates (60 mAh g^{-1} and 0.07 mV s^{-1}, respectively). Galvanostatic cycling at faster rates revealed that exfoliated graphite exhibited ca. 15%–20% higher discharge capacity retention, compared to pristine graphite, at rates ranging from 240 mA g^{-1} to up to 3.8 A g^{-1}. Variable-rate CV analyses establish that $AlCl_4^-$ electrochemical intercalation into graphite exhibits significant pseudocapacitive character associated with non-diffusion-limited ion intercalation processes. For the highest potential charge/discharge redox couple (2.35 V/2.2 V), exfoliated graphite exhibited significant pseudocapacitive contributions, while pristine graphite exhibited pure diffusion-limited Faradaic behavior. EIS measurements confirmed the interplay of pseudocapacitive and diffusion-limited Faradaic intercalation processes that vary with cell potential and graphite type, revealing significantly decreased interfacial charge-transfer resistances and higher apparent ion diffusion coefficients for exfoliated graphite. The significant differences in rate performance upon graphite exfoliation are due to differences in ion mass transport in the electrolyte phase within the porous electrode structure, which are shown to play a critical role at higher potentials and faster cycling rates. Structurally, exfoliation enhances ion mass transport in the porous electrode and hence rate performance by reducing its tortuosity. We hypothesize that increased electrolyte accessibility of interstitial pores and fewer blocked edge sites also facilitate ion mass transfer. The results underscore the beneficial effects of a scalable mild exfoliation process that enables higher-rate applications while preserving specific energy at lower rates. Future efforts to enhance the high-rate performance of graphite electrodes should focus on further enhancing the pseudocapacitive intercalation of $AlCl_4^-$ anions into graphite by continuing to reduce diffusion limitations, ideally using scalable and economical methods that enable electrodes with practical graphite mass loadings and electrode densities.

Acknowledgments

The authors gratefully acknowledge support from the U.S. National Science Foundation (NSF) under grant number CBET-170692 and funding from the U.S. National Aeronautics and Space Administration (NASA) via the NASA-CCNY Center for Advanced Batteries for Space under grant number 80NSSC19M0199. The authors thank Dr. Marc Florent and Prof. Teresa Bandosz (The City College of New York) for assistance with N_2 sorption measurements. Electron microscopy measurements were performed at the Imaging and Surface Science Facilities of the City University of New York (CUNY) Advanced Science Research Center.

ORCID

Jeffrey H. Xu https://orcid.org/0000-0003-3404-4194
Theresa Schoetz https://orcid.org/0000-0002-0016-4238
Robert J. Messinger https://orcid.org/0000-0002-5537-3870

References

1. M.-C. C. Lin et al., "An ultrafast rechargeable aluminium-ion battery." *Nature*, **520**, 324 (2015).
2. C.-J. Pan, C. Yuan, G. Zhu, Q. Zhang, C.-J. Huang, M.-C. Lin, M. Angell, B.-J. Hwang, P. Kaghazchi, and H. Dai, "An Operando X-ray diffraction study of chloroaluminate anion-graphite intercalation in aluminum batteries." *Proc. Natl Acad. Sci.*, **115**, 5670 (2018).
3. H. Sun, W. Wang, Z. Yu, Y. Yuan, S. Wang, and S. Jiao, "A new aluminium-ion battery with high voltage, high safety and low cost." *Chem. Commun.*, **51**, 11892 (2015).
4. K. V. Kravchyk, S. Wang, L. Piveteau, and M. V. Kovalenko, "Efficient aluminum chloride–natural graphite battery." *Chem. Mater.*, **29**, 4484 (2017).
5. H. Chen, H. Xu, S. Wang, T. Huang, J. Xi, S. Cai, F. Guo, Z. Xu, W. Gao, and C. Gao, "Ultrafast all-climate aluminum-graphene battery with quarter-million cycle life." *Sci. Adv.*, **3**, eaao7233 (2017).
6. J. H. Xu, D. E. Turney, A. L. Jadhav, and R. J. Messinger, "Effects of graphite structure and ion transport on the electrochemical properties of rechargeable aluminum-graphite batteries." *ACS Appl. Energy Mater.*, **2**, 7799 (2019).
7. D. Y. Wang et al., "Advanced rechargeable aluminium ion battery with a high-quality natural graphite cathode." *Nat. Commun.*, **8**, 14283 (2017).
8. X. Shen, T. Sun, L. Yang, A. Krasnoslobodtsev, R. Sabirianov, M. Sealy, W. N. Mei, Z. Wu, and L. Tan, "Ultra-fast charging in aluminum-ion batteries: electric double layers on active anode." *Nat. Commun.*, **12**, 1 (2021).
9. H. Huang, F. Zhou, P. Lu, X. Li, P. Das, X. Feng, K. Müllen, and Z. S. Wu, "Design and construction of few-layer graphene cathode for ultrafast and high-capacity aluminum-ion batteries." *Energy Storage Mater.*, **27**, 396 (2020).
10. S. K. Das, "Graphene: a cathode material of choice for aluminum-ion batteries." *Angew. Chemie - Int. Ed.*, **57**, 16606 (2018).
11. A. Ejigu, L. W. Le Fevre, K. Fujisawa, M. Terrones, A. J. Forsyth, and R. A. W. Dryfe, "Electrochemically exfoliated graphene electrode for high performance rechargeable chloroaluminate and dual ion batteries." *ACS Appl. Mater. Interfaces*, **11**, 23261 (2019).
12. S. C. Jung, Y. J. Kang, D. J. Yoo, J. W. Choi, and Y. K. Han, "Flexible few-layered graphene for the ultrafast rechargeable aluminum-ion battery." *J. Phys. Chem. C*, **120**, 13384 (2016).
13. D. C. Grahame, "Properties of the electrical double layer at a mercury surface. I. methods of measurement and interpretation of results." *J. Am. Chem. Soc.*, **63**, 1207 (1941).
14. S. Trasatti and G. Buzzanca, "Ruthenium Dioxide: a new interesting electrode material. Solid state structure and electrochemical behaviour." *J. Electroanal. Chem.*, **29**, A1 (1971).
15. S. Fleischmann, J. B. Mitchell, R. Wang, C. Zhan, D. E. Jiang, V. Presser, and V. Augustyn, "Pseudocapacitance: from fundamental understanding to high power energy storage materials." *Chem. Rev.*, **120**, 6738 (2020).
16. T. Schoetz, M. Kurniawan, M. Stich, R. Peipmann, I. Efimov, A. Ispas, A. Bund, C. Ponce De Leon, and M. Ueda, "Understanding the charge storage mechanism of conductive polymers as hybrid battery-capacitor materials in ionic liquids by: *In Situ* atomic force microscopy and electrochemical quartz crystal microbalance studies." *J. Mater. Chem. A*, **6**, 17787 (2018).
17. E. Frackowiak, "F. B. Carbon materials for the electrochemical storage of energy in capacitors." *J. Carbon*, **39**, 937 (2001).
18. M. D. Levi and D. Aurbach, "The mechanism of lithium intercalation in graphite film electrodes in aprotic media. Part 1. High resolution slow scan rate cyclic voltammetric studies and modeling." *J. Electroanal. Chem.*, **421**, 79 (1997).
19. S. Takahashi, N. Koura, S. Kohara, M.-L. Saboungi, and L. A. Curtiss, "Technological and scientific issues of room-temperature molten salts." *Plasmas Ions*, **2**, 91 (1999).
20. N. Canever, F. R. Hughson, and T. Nann, "Solid-electrolyte interphases (SEI) in nonaqueous aluminum-ion batteries." *ACS Appl. Energy Mater.*, **3**, 3673 (2020).
21. G. Kamath, B. Narayanan, and S. K. R. S. Sankaranarayanan, "Atomistic origin of superior performance of ionic liquid electrolytes for Al-Ion batteries." *Phys. Chem. Chem. Phys.*, **16**, 20387 (2014).
22. J. Wang, J. Polleux, J. Lim, and B. Dunn, "Pseudocapacitive contributions to electrochemical energy storage in TiO $_2$ (Anatase) nanoparticles." *J. Phys. Chem. C*, **111**, 14925 (2007).
23. J. H. Xu, A. L. Jadhav, D. E. Turney, and R. J. Messinger, "Molecular-level environments of intercalated chloroaluminate anions in rechargeable aluminum-graphite batteries revealed by solid-state NMR spectroscopy." *J. Mater. Chem. A*, **8**, 16006 (2020).
24. P. Bhauriyal, A. Mahata, and B. Pathak, "The staging mechanism of $AlCl_4-$ intercalation in a graphite electrode for an aluminium-ion battery." *Phys. Chem. Chem. Phys.*, **19**, 7980 (2017).
25. M. S. Wu, B. Xu, L. Q. Chen, and C. Y. Ouyang, "Geometry and fast diffusion of $AlCl_4$ cluster intercalated in graphite." *Electrochim. Acta*, **195**, 158 (2016).
26. M. S. Wu, B. Xu, and C. Y. Ouyang, "Further discussions on the geometry and fast diffusion of $AlCl_4$ cluster intercalated in graphite." *Electrochim. Acta*, **223**, 137 (2017).
27. Q. Wang, D. Zheng, L. He, and X. Ren, "Cooperative effect in a graphite intercalation compound: enhanced mobility of $AlCl_4$ in the graphite cathode of aluminum-ion batteries." *Phys. Rev. Appl.*, **12**, 1 (2019).
28. J. J. Giner-Sanz, E. M. Ortega, and V. Pérez-Herranz, "Optimization of the perturbation amplitude for EIS measurements using a total harmonic distortion based method." *J. Electrochem. Soc.*, **165**, E488 (2018).
29. M. Thommes, K. Kaneko, A. V. Neimark, J. P. Olivier, F. Rodriguez-Reinoso, J. Rouquerol, and K. S. W. Sing, "Physisorption of gases, with special reference to the evaluation of surface area and pore size distribution (IUPAC technical report)." *Pure Appl. Chem.*, **87**, 1051 (2015).
30. L. Stobinski, B. Lesiak, A. Malolepszy, M. Mazurkiewicz, B. Mierzwa, J. Zemek, P. Jiricek, and I. Bieloshapka, "Graphene oxide and reduced graphene oxide studied by the XRD, TEM and electron spectroscopy methods." *J. Electron Spectros. Relat. Phenomena*, **195**, 145 (2014).
31. R. Blume, D. Rosenthal, J. P. Tessonnier, H. Li, A. Knop-Gericke, and R. Schlögl, "Characterizing graphitic carbon with X-ray photoelectron spectroscopy: a step-by-step approach." *ChemCatChem*, **7**, 2871 (2015).
32. M. Phaner-Goutorbe, A. Sartre, and L. Porte, "Soft oxidation of graphite studied by XPS and STM." *Microsc. Microanal. Microstruct.*, **5**, 283 (1994).
33. G. A. Elia, G. Greco, P. H. Kamm, F. García-Moreno, S. Raoux, and R. Hahn, "Simultaneous X-ray diffraction and tomography operando investigation of aluminum/graphite batteries." *Adv. Funct. Mater.*, **2003913**, 1 (2020).
34. H. Lindström, S. Södergren, A. Solbrand, H. Rensmo, J. Hjelm, A. Hagfeldt, and S.-E. Lindquist, "Li^+ Ion Insertion in TiO_2 (Anatase). 2. Voltammetry on nanoporous films." *J. Phys. Chem. B*, **101**, 7717 (1997).
35. E. Barsoukov and J. R. Macdonald, *Impedance Spectroscopy*, ed. E. Barsoukov and J. R. Macdonald (Wiley, New York, NY) (2005).
36. R. Cabanel, G. Barral, J. P. Diard, B. Le Gorrec, and C. Montella, "Determination of the diffusion coefficient of an inserted species by impedance spectroscopy: application to the H/HxNb2O5 system." *J. Appl. Electrochem.* (1993)**23**, 93.
37. A. Lasia, *Electrochemical Impedance Spectroscopy and Its Applications* (Springer, Berlin) 1st ed. (2014).
38. P. Cördoba-Torres, T. J. Mesquita, and R. P. Nogueira, "Relationship between the origin of constant-phase element behavior in electrochemical impedance spectroscopy and electrode surface structure." *J. Phys. Chem. C*, **119**, 4136 (2015).
39. M. D. Levi, C. Wang, and D. Aurbach, "Two parallel diffusion paths model for interpretation of PITT and EIS responses from non-uniform intercalation electrodes." *J. Electroanal. Chem.*, **561**, 1 (2004).
40. A. J. Bard and L. R. Faulkner, *Electrochemical Methods: Fundamentals and Applications* (Wiley, New Jersey, NJ) (2001).
41. R. B. MacMullin and G. A. Muccini, "Characteristics of porous beds and structures." *AIChE J.*, **2**, 393 (1956).
42. M. Salanne, L. J. A. Siqueira, A. P. Seitsonen, P. A. Madden, and B. Kirchner, "From molten salts to room temperature ionic liquids: simulation studies on chloroaluminate systems." *Faraday Discuss.*, **154**, 171 (2012).